

Surrogate modeling for uncertainty quantification in nonlinear dynamics

Stefano Marelli^{*1}, Styfen Schär^{†1}, and Bruno Sudret^{‡1}

¹Chair of Risk, Safety and Uncertainty Quantification, ETH Zürich, Switzerland

July 1st, 2025

Abstract

When faced with the task of predicting the behavior of a complex system, engineers have to deal with incomplete knowledge on its effective operating conditions: the loads it will be subjected to, unexpected environmental and climatic condition, manufacturing uncertainties, and more. As a consequence, uncertainty quantification (UQ) has become a staple tool in modern modeling-based engineering. From identifying and characterizing multiple sources of uncertainty, to quantitatively assessing their effect on the accuracy and reliability of the corresponding model predictions, UQ offers a vast arsenal of algorithms and methodologies.

Due to the stochastic nature of uncertainty, however, most of these techniques require a large number of evaluations of one or more computational models that represent the system. These models can be computationally demanding, especially for complex engineering systems, to the point that the available computational resources often constrain the spectrum of feasible UQ analyses. It is therefore not surprising that surrogate models, *i.e.* powerful functional proxies that rely on a relatively small set of training data, have taken center stage in the state-of-the art in UQ.

This book chapter offers a concise review of the state-of-the-art in surrogate modeling for uncertainty quantification, with a particular emphasis on the challenging task of approximating the full time-dependent response of dynamical systems. Time-dependent problems are classified into several categories based on the intrinsic complexity of the input excitation. Correspondingly, the chapter presents methods that combine principal component analysis with polynomial chaos expansions, as well as approaches involving time warping and nonlinear autoregressive models with exogenous inputs (NARX models). Each method is illustrated through simple application examples that help clarify the various approaches.

^{*}marelli@ibk.baug.ethz.ch

[†]styfen.schaer@ibk.baug.ethz.ch

[‡]sudret@ethz.ch

Contents

1	Introduction to uncertainty quantification	3
2	Surrogate models for time-independent problems	3
2.1	Classical families of surrogates	3
2.2	Training and validation of classical surrogates	4
2.3	Sparse polynomial chaos expansions	5
3	Surrogate modeling for “simple” dynamical systems	6
3.1	Classes of dynamical systems	6
3.2	Problems with fundamentally simple inputs	6
3.3	Time warping	8
3.3.1	Introduction	8
3.3.2	Stochastic time warping	9
3.3.3	Application: nonlinear Bouc-Wen oscillator	10
3.3.4	Conclusions	12
4	Auto-regressive models	12
4.1	Introduction	12
4.2	Training and prediction with NARX models	13
4.3	Limitations of NARX modeling	15
4.4	Polynomial-chaos NARX	16
4.5	Manifold-NARX	17
5	Application to a simple case study: coupled oscillator	18
6	Conclusions	23

1 Introduction to uncertainty quantification

Computational models used in engineering sciences aim at mimicking the behaviour of a real system *in silico* by numerically solving its governing equations, which are usually partial differential equations. After some time- and space- discretization of the latter, the problem boils down to solving a possibly large set of linear or nonlinear equations, leading to a vector of quantities of interest (QoI) (a.k.a. model response) $\mathbf{y} \in \mathbb{R}^Q$. The input parameters that characterize the system, *i.e.* its geometrical dimensions, material properties, external loading or operating conditions, can be gathered in a vector $\mathbf{x} \in \mathcal{D}_X \subset \mathbb{R}^M$. With this notation, the computational model \mathcal{M} that predicts the QoIs for each vector of input parameters can be seen as a mapping $\mathcal{M} : \mathbf{x} \mapsto \mathbf{y} = \mathcal{M}(\mathbf{x})$. In practice, such mapping is rarely analytical, apart for academic examples. Usually, computing \mathbf{y} for a given \mathbf{x}_0 requires running a computer code (*e.g.* a finite element software in engineering mechanics), a single run of which may take minutes to hours for a high-fidelity model.

In the context of uncertainty quantification, the input parameters are not perfectly known, and modelled accordingly by a random vector \mathbf{X} of prescribed probability density function (PDF) $f_{\mathbf{X}}$, which is built using expert knowledge, existing data (through statistical inference), or both. Uncertainty propagation aims at characterizing the statistical properties of the resulting response random vector $\mathbf{Y} = \mathcal{M}(\mathbf{X})$. Monte Carlo simulation, the most intuitive method that allow one to carry out such an analysis, is based on sampling a (usually large) set of input parameters $\mathcal{X} = \{\mathbf{x}_1, \dots, \mathbf{x}_{n_{\text{MCS}}}\}$ and running the model \mathcal{M} for each sample. The resulting set of model responses can then be post-processed to compute statistical moments, quantiles, probabilities of exceedence or sensitivity indices.

Models of dynamical systems, often central to engineering applications, are a particular case of computational models, where \mathbf{Y} , and often also \mathbf{X} , are time-dependent. In this case, the model can be seen as a mapping from the input vector $\mathbf{x} \in \mathbb{R}^M$ and time $t \in \mathbb{R}$ to the model response $\mathbf{y} \in \mathbb{R}^Q$:

$$\mathcal{M} : (\mathbf{x}, t) \mapsto \mathbf{y}(t) = \mathcal{M}(\mathbf{x}, t), \quad (1)$$

with $t \in [0, T]$ for applications with finite duration T . In practice, time is discretized to be computationally tractable, with $\mathcal{T} = \{t_1, \dots, t_Q\}$, leading to a vector model output $\mathbf{y} = (\mathcal{M}(\mathbf{x}, t_1), \dots, \mathcal{M}(\mathbf{x}, t_Q))^{\top}$.

2 Surrogate models for time-independent problems

2.1 Classical families of surrogates

The use of brute-force approaches such as Monte Carlo simulation for uncertainty propagation, or genetic algorithms for optimization, is usually intractable when each run of the model \mathcal{M} already requires a significant computational time. To bypass this problem, *surrogate models*

have emerged in the last three decades. Surrogate models are analytical functions selected in a certain family, which approximate the original model while being extremely fast to evaluate. More precisely, a surrogate is a mapping $\widehat{\mathcal{M}} : \mathbf{x} \in \mathbb{R}^M \mapsto \widehat{\mathbf{y}} \in \mathbb{R}^Q$ that satisfies (in some sense to be precised):

$$\mathcal{M}(\mathbf{x}) \approx \widehat{\mathcal{M}}(\mathbf{x}). \quad (2)$$

In Table 1 the most common families of surrogates are listed together with their functional shape and parameters, namely polynomial chaos expansions (PCE) (Ghanem and Spanos, 2003; Xiu and Karniadakis, 2002; Xiu, 2010), low-rank tensor approximations (Doostan et al., 2013; Chevreuil et al., 2015; Konakli and Sudret, 2016a,b), Gaussian processes (a.k.a. Kriging) (Santner et al., 2003; Rasmussen and Williams, 2006), support vector machines (Smola and Schölkopf, 2004), and (deep) neural networks (Murphy, 2012; Goodfellow et al., 2016). In this chapter, we will focus on polynomial chaos expansions, which are presented in more detail below.

Table 1: Most common families of surrogate models used for uncertainty quantification

Name	Shape	Parameters
Polynomial chaos expansions	$\widehat{\mathcal{M}}(\mathbf{x}) = \sum_{\alpha \in \mathcal{A}} a_{\alpha} \Psi_{\alpha}(\mathbf{x})$	a_{α}
Low-rank tensor approximations	$\widehat{\mathcal{M}}(\mathbf{x}) = \sum_{l=1}^R b_l \left(\prod_{i=1}^M \left(\sum_{k=0}^{p_i} z_{k,l}^{(i)} \phi_k^{(i)}(x_i) \right) \right)$	\mathbf{b}, \mathbf{z}
Kriging (a.k.a Gaussian processes)	$\widehat{\mathcal{M}}(\mathbf{x}) = \boldsymbol{\beta}^T \cdot \mathbf{f}(\mathbf{x}) + \sigma_Z Z(\mathbf{x}, \omega)$	$\boldsymbol{\beta}, \sigma_Z^2, \boldsymbol{\theta}$
Support vector machines	$\widehat{\mathcal{M}}(\mathbf{x}) = \sum_{i=1}^M a_i K(\mathbf{x}_i, \mathbf{x}) + b$	\mathbf{a}, b
(Deep) Neural networks	$\widehat{\mathcal{M}}(\mathbf{x}) = f_n(\cdots f_2(b_2 + f_1(b_1 + \mathbf{w}_1 \cdot \mathbf{x}) \cdot \mathbf{w}_2))$	\mathbf{w}, \mathbf{b}

2.2 Training and validation of classical surrogates

Each type of surrogate depends on parameters generically denoted by $\boldsymbol{\theta} \in \mathbb{R}^{n_{\theta}}$ (see Table 1, 3rd column), which are explicitly shown in the notation $\widehat{\mathcal{M}}(\mathbf{x}; \boldsymbol{\theta})$. The latter are fitted from simulated data, *i.e.* an *experimental design* (ED) $\mathcal{X}_{\text{ED}} = \{\mathbf{x}^{(1)}, \dots, \mathbf{x}^{(n_{\text{ED}})}\}$ and the corresponding model evaluations $\mathcal{Y}_{\text{ED}} = \{y^{(1)}, \dots, y^{(n_{\text{ED}})}\}$ with $y^{(i)} = \mathcal{M}(\mathbf{x}^{(i)})$, $i = 1, \dots, n_{\text{ED}}$.¹ More specifically, a *loss function* such as the mean-square error is introduced to quantify the discrepancy between the model and its surrogate over the DOE, and minimized over the parameters $\boldsymbol{\theta}$:

$$\begin{aligned} \widehat{\boldsymbol{\theta}} &= \arg \min_{\boldsymbol{\theta}} \mathcal{L}(\mathcal{Y}_{\text{ED}}, \widehat{\mathcal{M}}(\mathcal{X}_{\text{ED}})) \\ &= \arg \min_{\boldsymbol{\theta}} \frac{1}{n_{\text{ED}}} \sum_{i=1}^{n_{\text{ED}}} (y^{(i)} - \widehat{\mathcal{M}}(\mathbf{x}^{(i)}; \boldsymbol{\theta}))^2. \end{aligned} \quad (3)$$

The accuracy of the surrogate is usually evaluated using a *test set* of n_{test} points sampled in the input space, and their associated model responses.

¹We assume here that the output QoI is scalar for simplicity, *i.e.* $Q = 1$.

2.3 Sparse polynomial chaos expansions

Following the pioneering work of [Ghanem and Spanos \(1991\)](#) and [Xiu and Karniadakis \(2002\)](#), polynomial chaos expansions have become one of the most popular surrogate modeling techniques for uncertainty quantification. Assuming that the input random vector \mathbf{X} has M independent components (X_1, \dots, X_M), and that $Y = \mathcal{M}(\mathbf{X})$ has a finite variance, the following expansion holds:

$$Y = \sum_{\alpha \in \mathbb{R}^M} c_\alpha \psi_\alpha(\mathbf{X}), \quad (4)$$

where α are multi-indices and $\{\psi_\alpha, \alpha \in \mathbb{R}^M\}$ are multivariate polynomials in the input variables defined as

$$\psi_\alpha(\mathbf{X}) \stackrel{\text{def}}{=} \prod_{i=1}^M \psi_{\alpha_i}^{(i)}(x_i). \quad (5)$$

Denoting by f_{X_i} the marginal PDF of the i -th input random variable over its support \mathcal{D}_{X_i} , the univariate polynomials $\{\psi_k^{(i)}, k \in \mathbb{N}\}$ are orthogonal *w.r.t.* the probability measure induced by X_i and satisfy:

$$\int_{\mathcal{D}_{X_i}} \psi_j^{(i)}(x) \psi_k^{(i)}(x) f_{X_i}(x) dx = \delta_{jk}, \quad (6)$$

where δ_{jk} is the Kronecker symbol equal to 1 if $j = k$ and 0 otherwise. Due to the tensor product construction in Eq. (5), the multivariate polynomials inherit from the orthogonality property:

$$\mathbb{E}_{\mathbf{X}} [\psi_\alpha(\mathbf{X}) \psi_\beta(\mathbf{X})] = \int_{\mathcal{D}_{\mathbf{X}}} \psi_\alpha(\mathbf{x}) \psi_\beta(\mathbf{x}) f_{\mathbf{X}}(\mathbf{x}) d\mathbf{x} = \delta_{\alpha\beta}, \quad (7)$$

with $\delta_{\alpha\beta} = 1$ if $\alpha = \beta$ and 0 otherwise.

After selecting a truncation scheme $\mathcal{A} \subset \mathbb{R}^M$, *e.g.*, all polynomials with *total degree* $\|\alpha\|_1 \leq p$, the coefficients $\hat{\mathbf{c}} \stackrel{\text{def}}{=} (c_\alpha, \alpha \in \mathcal{A})$ can be computed by ordinary least squares. Denoting by Ψ the information matrix defined by:

$$\Psi_{ij} = \Psi_{\alpha_j}(\mathbf{x}^{(i)}), \quad i = 1, \dots, n_{\text{ED}}, \quad j = 1, \dots, \text{card}(\mathcal{A}), \quad (8)$$

where α_j is the j -th multi-index of \mathcal{A} following the lexicographic ordering, the PCE coefficients are obtained from Eq. (3) as:

$$\hat{\mathbf{c}} = \arg \min_{c_\alpha \in \mathbb{R}^{\text{card}(\mathcal{A})}} \frac{1}{n_{\text{ED}}} \sum_{i=1}^{n_{\text{ED}}} \left(y^{(i)} - \sum_{\alpha \in \mathcal{A}} c_\alpha \psi_\alpha(\mathbf{x}^{(i)}) \right)^2. \quad (9)$$

In practice, the relevant truncation scheme is problem-specific and not known in advance. Modern solvers such as least-angle regression ([Efron et al., 2004](#); [Blatman and Sudret, 2011](#)) extract a sparse expansion from a *candidate* truncated basis, before the (nonzero) coefficients are computed by ordinary least-squares. For recent developments on sparse PCEs, the reader is referred to [Lüthen et al. \(2021, 2022\)](#).

3 Surrogate modeling for “simple” dynamical systems

3.1 Classes of dynamical systems

Extending any of the surrogate modeling techniques in Table 1 to handle dynamical systems is usually not straightforward. As a general rule, the complexity of the computational model (Eq. (2)) tends to increase rapidly with time (Wan and Karniadakis, 2005; Le Maître et al., 2010; Choi et al., 2014; Mai, 2016).

We consider here two main classes of problems, distinguished by their input characteristics, that are treated with entirely different surrogate modeling strategies: those with *fundamentally simple* inputs, and those with *fundamentally complex* inputs. This distinction, first introduced in Meles et al. (2025) and Schär (2025), refers to the intrinsic dimensionality of the input excitation:

- *fundamentally simple inputs* can be accurately represented by a finite and fixed number of scalar parameters, typically $O(10)$. These can either be time-independent parameter vectors typical of classical surrogate models (see Section 2), or simple time-series with limited frequency content, such as monochromatic sinusoidal waves, or superpositions thereof, which can be easily parameterized with a small number of frequency amplitudes and phases.
- *fundamentally complex inputs* do not generally admit compact and/or fixed representations, and generally present a much richer frequency/information content. Common examples of this type of inputs are found in stochastic earthquake models (Rezaeian and Der Kiureghian, 2010), or turbulent wind fields (Jonkman, 2009).

The first class of inputs can be generally handled by extending classical surrogate modeling strategies to vector outputs, in some cases with additional preprocessing steps to homogenize the input. These approaches are presented in detail in Sections 3.2 and 3.3.

The second class of inputs requires instead an entirely different surrogate modeling paradigm, namely auto-regressive modeling, which will be introduced in Section 4.

3.2 Problems with fundamentally simple inputs

The derivation of polynomial chaos expansions of a scalar output quantity of interest (Section 2.3) can be easily extended to a vector \mathbf{y} with Q components, where the procedure described in Section 2.2 is simply applied component by component. For dynamical systems, a naive approach consists in considering each (discretized) output trajectory as a vector (where each component is attached to a particular time instant of the simulation) and use PCE for each component, *i.e.* at each time instant. When considering a pre-defined fix basis of polynomials, the solution of the OLS in Eq. (9) only requires a single matrix inversion, and then a matrix-vector product for each output component. When considering *sparse solvers* though,

the optimal sparse basis may be different for each output $\{y_q, q = 1, \dots, Q\}$, leading to a high computational cost when $Q = \mathcal{O}(10^{3-4})$.

Because the computed trajectories for problems with fundamentally simple inputs are similar, a pre-processing step can be used. *Principal component analysis* (Jolliffe, 2002) is applied to the n_{ED} trajectories, and only a small number of components $m \ll \min(n_{\text{ED}}, Q)$ allows us to represent the data accurately.

Given the experimental $(n_{\text{ED}} \times Q)$ -matrix $\mathcal{Y}_{\text{ED}} \equiv (\mathbf{y}^{(1)}; \dots; \mathbf{y}^{(n_{\text{ED}})})$, the principal component analysis is carried out as follows:

- The *mean output* $\bar{\mathbf{y}}$ and *empirical covariance matrix* $\widehat{\Sigma}_{\mathbf{Y}}$ are first computed:

$$\begin{aligned}\bar{\mathbf{y}} &= \frac{1}{n_{\text{ED}}} \sum_{i=1}^{n_{\text{ED}}} \mathbf{y}^{(i)}, \\ \widehat{\Sigma}_{\mathbf{Y}} &= \frac{1}{n_{\text{ED}} - 1} \sum_{p=1}^{n_{\text{ED}}} (\mathbf{y}_i^{(p)} - \bar{\mathbf{y}}_i) (\mathbf{y}_j^{(p)} - \bar{\mathbf{y}}_j).\end{aligned}\tag{10}$$

- The eigenvalue decomposition of matrix $\widehat{\Sigma}_{\mathbf{Y}}$ is carried out. The eigenvectors (“eigenmodes”) are denoted by $\{\phi_j, j = 1, \dots, Q\}$. By construction they are normalized. Only the m largest eigenvalues and related eigenmodes are kept.
- For each original Q -dimensional vector $\mathbf{y}^{(i)}$, the *score coefficients* $\{z_j^{(i)}, j = 1, \dots, m\}$ are computed by *projection* onto the eigenmodes $\{\phi_j, j = 1, \dots, m\}$:

$$z_j^{(i)} = \phi_j^T (\mathbf{y}^{(i)} - \bar{\mathbf{y}}).\tag{11}$$

Note that these score coefficients have a zero mean value by construction. They correspond to the projection coefficients of the original response vector onto the new basis defined by the eigenvectors of $\Sigma_{\mathbf{Y}}$.

From this projection, we obtain a new dataset comprising n_{ED} realizations of score vectors of length m . Independent sparse polynomial chaos expansions of each variable $\{Z_j, j = 1, \dots, m\}$ are then computed:

$$Z_j \approx \sum_{\alpha \in \mathcal{A}_j} \zeta_{\alpha,j} \Psi_{\alpha}(\mathbf{X}),\tag{12}$$

where $\zeta_{\alpha,j}$ is the PCE coefficient of polynomial Ψ_{α} of the j -th score variable Z_j . Finally, these PCEs can be recombined to provide a prediction for the whole curve, for a new input vector \mathbf{x}^* :

$$\widehat{\mathcal{M}}(\mathbf{x}^*) = \bar{\mathbf{y}} + \sum_{j=1}^m \sum_{\alpha \in \mathcal{A}_j} \zeta_{\alpha,j} \Psi_{\alpha}(\mathbf{x}^*) \phi_j.\tag{13}$$

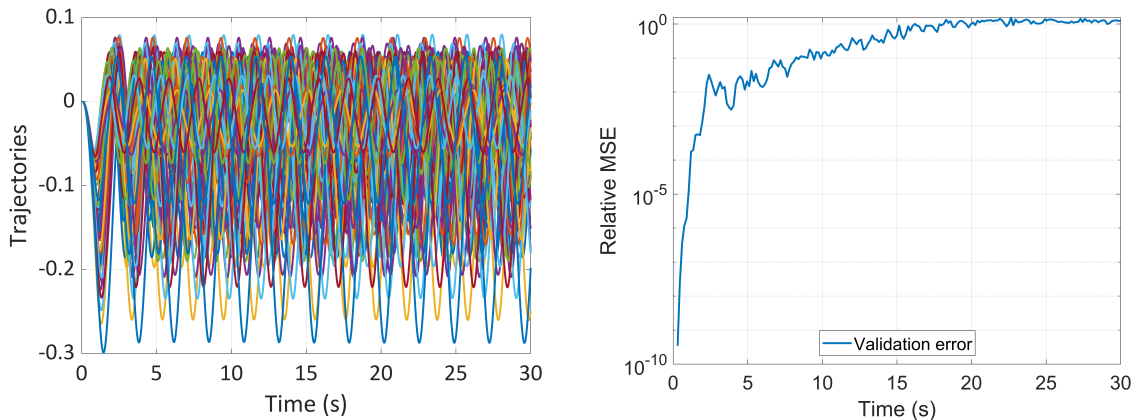
The number m of components retained is usually chosen so as to explain the $(1 - \epsilon)$ fraction of the empirical variance of the experimental matrix, with $\epsilon = 1 - 5\%$. This is obtained by taking the m largest eigenvalues so that their sum is greater than $(1 - \epsilon) \cdot \text{trace}(\widehat{\Sigma}_{\mathbf{Y}})$

Such a procedure was first introduced by [Blatman and Sudret \(2013\)](#) together with sparse PCEs. It is generally known as *model order reduction*, *proper orthogonal decomposition* or simply *singular value decomposition*. Applications to time-dependent problems with fundamentally simple inputs can be found in [Nagel et al. \(2020\)](#) and [Wagner et al. \(2020\)](#), among others. Recent works also use PCA in combination with other surrogates to handle problems with very high-dimensional, correlated responses, see, *e.g.* [Aversano et al. \(2019\)](#) and [Guo et al. \(2023\)](#).

3.3 Time warping

3.3.1 Introduction

The combination of principal component analysis and sparse polynomial chaos expansion presented in the previous section gives accurate results when the set of training trajectories show some simple common structure. However, when considering as an example (damped) oscillating systems whose characteristics are uncertain, the output trajectories may typically look like the ones in Figure 1a ([Mai and Sudret \(2017\)](#)): each curve oscillates at its own frequency and phase, so that when considering a particular *frozen* time instant t^* , the outputs $\{y^{(i)}(t^*), i = 1, \dots, n_{ED}\}$ show a complex distribution, since some realizations correspond to a peak of the trajectory, some to a valley, and others to anything in between ([Mai, 2016](#)). When applying sparse PCE at each time instant (*i.e.*, considering each trajectory as a Q -dimensional vector and using a PCE for each component as outlined in Section 3.2), which we call *time-frozen* PCE, the point-in-time validation error rapidly blows up, as shown in Figure 1b. Note that the pre-processing step using principal component analysis, which is a mere *linear transform*, does not solve the problem.



(a) A hundred trajectories in the original (com- (b) Evolution of the validation error using time-
mon) time scale t frozen polynomial chaos expansion

Figure 1: Bouc-Wen oscillator with random input parameters under sinusoidal forcing (after [Mai and Sudret \(2017\)](#)).

To capture the increasing complexity of the input-output mapping at large time horizons,

diverse intrusive and nonintrusive techniques have been proposed (Sapsis and Lermusiaux, 2009; Gerritsma et al., 2010; Le Maître et al., 2010; Choi et al., 2014; Luchtenburg et al., 2014). In this section, we present a fully nonintrusive technique based on *stochastic time warping*, as developed in Mai and Sudret (2017), following an original idea by Le Maître et al. (2010) in an intrusive context.

3.3.2 Stochastic time warping

Stochastic time warping can be seen as a preprocessing of the training trajectories in which each curve is *warped* so as to become “similar” to a reference curve y^{ref} , which is *e.g.*, the curve obtained from the mean-value input vector. Practically, in case of oscillatory systems, each trajectory $y^{(i)}(t) = \mathcal{M}(t, \mathbf{x}^{(i)})$ will be displayed along a new time axis $\tau(t, \mathbf{x}^{(i)})$, where the mapping $t \mapsto \tau = TW(t, \mathbf{x}^{(i)})$ is invertible for each realization. This time warping function TW is parametrized with a few coefficients, *e.g.*, a linear combination of given functions $f_j(t)$:

$$TW(t, \mathbf{x}) = \sum_{j=1}^{n_{\beta}} \beta_j(\mathbf{x}) f_j(t). \quad (14)$$

The *warped curve*, for a set of parameters β , is defined as:

$$y^{(i)}(\tau; \beta) = \mathcal{M}(TW^{-1}(\tau, \mathbf{x}^{(i)}; \beta), \mathbf{x}^{(i)}). \quad (15)$$

For each curve i , the optimal set of parameters β_i^* is computed so as to minimize a distance between the reference curve and the current warped realization:

$$\beta^{(i)} = \arg \min_{\beta \in \mathbb{R}^{|\beta|}} d\left(y^{(i)}(\tau; \beta), y^{\text{ref}}\right). \quad (16)$$

In the original publication of Mai and Sudret (2017), the time warping function is affine: $TW(t, \mathbf{x}) = kt + \phi$, that is $\beta = (k, \phi)$ or even linear $TW(t, \mathbf{x}) = kt$, $\beta \equiv k$, but more general formats could be used. The norm selected to measure the distance between two (warped) curves y_1 and y_2 was the cross-correlation over the time interval of interest $[0, T]$:

$$d(y_1(\cdot), y_2(\cdot)) = \frac{\left| \int_0^T y_1(s) y_2(s) \, ds \right|}{\sqrt{\int_0^T y_1^2(s) \, ds} \sqrt{\int_0^T y_2^2(s) \, ds}}. \quad (17)$$

Note that time warping usually rescales each trajectory on a different time interval, which requires reinterpolating them on a common time grid over a joint interval $[0, T]$, which requires explicit handling to ensure consistency (see Mai and Sudret (2017) for technical details).

The effect of applying time-warping to the Bouc-Wen non-linear oscillator example in Figure 1a is shown in Figure 2a. After warping, the training curves show remarkable similarity: sparse PCE could then be used at each time instant, as described in Section 3.2. For efficiency, principal component analysis can also be used on the warped curves prior to applying sparse PCE to their score coefficients.

The goal of constructing surrogates is to be able to rapidly emulate new trajectories for new input vectors \mathbf{x}^* . From the above construction, the prediction occurs *in the warped timescale*, meaning that the inverse of Eq. (14) should be used to compute the predicted trajectory *in the physical time*. To this aim, the warping coefficients $\beta(\mathbf{x}^*)$ are necessary. This is achieved by building sparse polynomial chaos expansions of each β_j using the experimental design of warping parameters \mathcal{Y}_β obtained from Eq. (16) from each trajectory:

$$\beta_j(\mathbf{X}) \approx \sum_{\alpha \in \mathcal{A}_j} b_{\alpha,j} \Psi_\alpha(\mathbf{X}), \quad j = 1, \dots, n_\beta. \quad (18)$$

As a summary, the time-warping-PCE surrogate modeling technique allows us to emulate the trajectory $y(\mathbf{x}^*)$ as follows:

- Compute the coefficients of the time warping function TW for \mathbf{x}^* as $\beta_j(\mathbf{x}^*) \approx \sum_{\alpha \in \mathcal{A}_j} b_{\alpha,j} \Psi_\alpha(\mathbf{x}^*)$
- Compute the *warped* trajectory $y^*(\tau; \beta^*)$ using PCA and sparse PCE, as in Eq. (13)
- Use the inverse of the time warping function to get the trajectory $y^*(TW^{-1}(\tau; \beta^*))$ in the physical time scale.

3.3.3 Application: nonlinear Bouc-Wen oscillator

To illustrate the whole approach, let us consider the single degree of freedom (SDOF) Bouc-Wen oscillator subject to a stochastic excitation. The equation of motion of the oscillator reads:

$$\begin{cases} \ddot{y}(t) + 2\zeta\omega\dot{y}(t) + \omega^2(\rho y(t) + (1 - \rho)z(t)) = -x(t), \\ \dot{z}(t) = \gamma\dot{y}(t) - \alpha|\dot{y}(t)||z(t)|^{n-1}z(t) - \beta\dot{y}(t)|z(t)|^n, \end{cases} \quad (19)$$

in which ζ is the damping ratio, ω is the fundamental frequency, $\rho = 0$ is the post- to pre-yield stiffness ratio, $\gamma = 1$, $n = 1$, α, β are parameters governing the hysteretic loops, and the excitation $x(t)$ is a sinusoidal function given by $x(t) = A \sin(\omega_x t)$. The parameters $\mathbf{X} = (\zeta, \omega, \alpha, A, \omega_x)$ are considered independent random variables, with associated distributions given in Table 2. A hundred realizations of trajectories have been already shown in Figure 1a.

Table 2: Uncertain parameters of the Bouc-Wen model.

Parameter	Distribution	Mean	Std. dev.
ζ	Uniform	0.02	0.002
ω	Uniform	2π	0.2π
α	Uniform	50	5
A	Uniform	1	0.1
ω_x	Uniform	π	0.1π

Using the training curves shown in Figure 1a, a linear time warping is applied to each trajectory, and the single coefficient β fitted for each of them is used to build a sparse PCE. The

100 curves after time warping are shown in Figure 2a. The surrogate obtained by coupling time warping, principal component analysis and sparse PCE is used to predict 10,000 new trajectories, which are used to estimate the empirical mean and standard deviation curves, shown in blue in Figure 2c-2d.

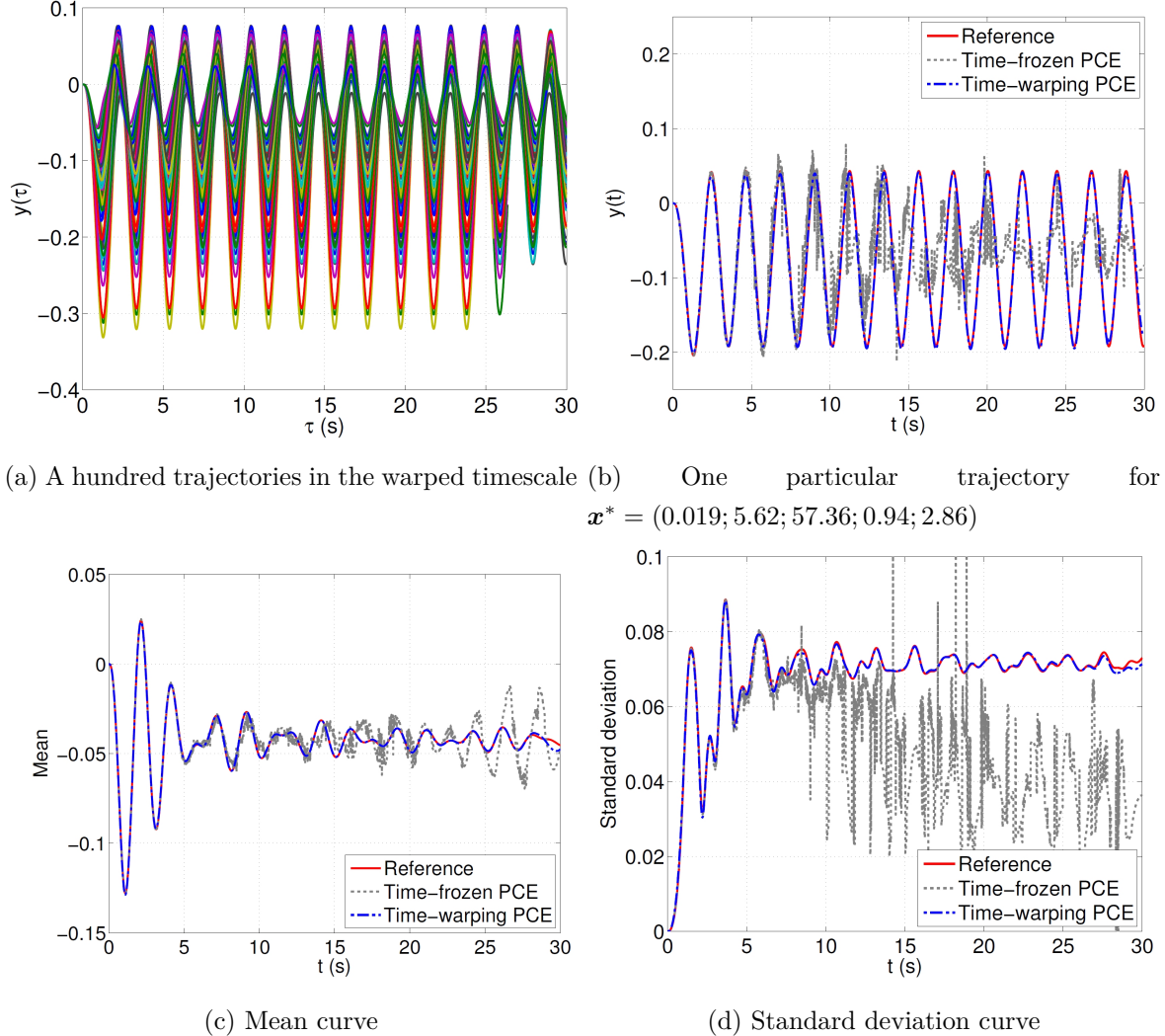


Figure 2: Surrogate model of Bouc-Wen oscillator trajectories with random parameters- and sinusoidal forcing (after [Mai and Sudret \(2017\)](#)).

In these figures, the curves predicted using time-frozen PCE are also plotted in grey, while reference curves obtained from 10^5 Monte Carlo samples are also plotted in red. The agreement between reference and time-warping-PCA-PCE is remarkable, while the time-frozen PCE show poor results after a few seconds. Finally, it is worth mentioning that this surrogate modeling approach delivers good accuracy not only for statistics, but also for each curve separately: Figure 2b shows a particular trajectory (plotted in red, obtained for the realization $\mathbf{x}^* = (0.0191; 5.6208; 57.3581; 0.9401; 2.8577)$ and the two surrogate curves obtained by time-warping-PCA-PCE and time-frozen PCE.

3.3.4 Conclusions

In the case of fundamentally simple inputs, surrogate models of dynamical systems can be constructed using sparse polynomial chaos expansions (PCE) coupled with appropriate pre-processing of the training trajectories. When the response trajectories are relatively similar in phase and frequency content, time-frozen PCE may be used effectively. The introduction of principal component analysis (PCA) does not improve the accuracy in such cases but can significantly reduce the computational cost: instead of fitting $Q = \mathcal{O}(10^{3-4})$ sparse PCEs, only a handful of $m = \mathcal{O}(10)$ sparse PCE need to be fitted.

Still, for some fundamentally simple inputs parameterized by a small number of random variables, the resulting trajectories – though similar in shape – may differ greatly in phase and frequency. In such cases, the *stochastic time warping* pre-processing step significantly improves surrogate accuracy. This warping has also been successfully applied in the frequency domain, where the curves of interest are frequency response functions. For such applications, a simple piecewise linear warping function is used to align the peaks and valleys of the curves with those of a reference curve, see [Yaghoubi et al. \(2017\)](#) for details.

4 Auto-regressive models

4.1 Introduction

Approximating the response of complex systems subject to external, fundamentally complex time-dependent loads (see Section 3.1) is a well-known challenge in many fields of model-based engineering. Examples include damage detection ([Mattson and Pandit, 2006](#); [Gao et al., 2016](#)), control systems ([Levin and Narendra, 1996](#); [Hu et al., 2024](#)), maintenance ([Langeron et al., 2021](#); [Samsuri et al., 2023](#)) and design optimization ([Yu et al., 2023](#); [Deshmukh and Allison, 2017](#)), among others. More recently, applications in the fields of uncertainty quantification ([Spiridonakos and Chatzi, 2015b,a](#); [Mai et al., 2016](#); [Schär et al., 2024](#)) and reliability analysis ([Garg et al., 2022](#); [Zhou and Li, 2023](#); [Zhang et al., 2024](#)) have started to emerge, due to the large number of model evaluations required for this type of analysis.

All these applications share a common tool: autoregressive models with exogenous inputs (ARX) ([Billings, 2013](#)). ARX models, together with their nonlinear variant NARX, are based on the assumption that the response of a complex system at any give time t is determined by the exogenous loading and the history of the system. Following the notation introduced in [Schär et al. \(2024\)](#), and considering a discretized time axis $\mathcal{T} = \{0, \delta t, 2\delta t, \dots, (Q-1)\delta t\}$ this is formalized as:

$$y(t) = \mathcal{M}(\mathbf{x}(\mathcal{T} \leq t), \boldsymbol{\beta}), \quad (20)$$

where a scalar response $y(t)$ is represented by a deterministic mapping \mathcal{M} on the M -dimensional exogenous input vector $\mathbf{x}(t) \in \mathbb{R}^M$, and the set of initial system state variables (or boundary

conditions) β . For the sake of notational simplicity, we will hereinafter drop the explicit dependence on β , unless required by the context. Additionally, we use the notation $\bullet(\mathcal{T} \leq t)$ to indicate that the represented quantity depends on the exogenous input only up to time t , but not on future times, to respect causality constraints.

Consistently with the general principles of surrogate modeling, the goal of autoregressive models is to approximate the response of the original computational model as:

$$\hat{y}(t) = \widehat{\mathcal{M}}(\mathbf{x}(\mathcal{T} \leq t), \beta) \approx \mathcal{M}(\mathbf{x}(\mathcal{T} \leq t), \beta). \quad (21)$$

To achieve the goal of Eq. (21), NARX defines the so-called *one-step-ahead* parametric map as:

$$\hat{y}(t + \delta t) = \widehat{\mathcal{M}}(\mathbf{x}(\mathcal{T} \leq t + \delta t), \mathbf{y}(\mathcal{T} < t + \delta t); \mathbf{c}) + \varepsilon(t), \quad (22)$$

where $\varepsilon(t) \sim \mathcal{N}(0, \sigma_\varepsilon(t))$ is a zero-mean residual term, often assumed Gaussian, and \mathbf{c} is a vector of real parameters that fully characterize the map $\widehat{\mathcal{M}}$. Eq. (22) includes all the ingredients at the basis of autoregressive models with exogenous inputs, as the response at the next time instant $t + \delta t$ depends on the exogenous input excitation until the next time instant $\mathbf{x}(\mathcal{T} \leq t + \delta t)$, but also on the past responses $\mathbf{y}(\mathcal{T} \leq t)$.

One of the advantages of the formulation in Eq. (22) is that there is no strict requirement on the functional form of the parametric map $\widehat{\mathcal{M}}(\bullet; \mathbf{c})$. This allows NARX models to be combined with many other techniques from the statistical regression and machine learning literature, from classical polynomial regression (Billings, 2013), to Gaussian process regression (Murray-Smith et al., 1999; Kocijan, 2012; Worden et al., 2018), neural networks (Siegelmann et al., 1997; Li et al., 2021; Song et al., 2022), support vector machines (Acuña et al., 2012; Ranković et al., 2014; Zhang et al., 2017), and many others (Aguirre and Billings, 1993; Coca and Billings, 2001; Chen et al., 2008).

4.2 Training and prediction with NARX models

We consider herein nonintrusive NARX models, *i.e.* the surrogate is trained on a finite-size set of full computational model evaluations, the experimental design \mathcal{X} :

$$\mathcal{X} = \left\{ \left(\mathbf{x}^{(i)}, \mathbf{y}^{(i)} \right), i = 1, \dots, n_{\text{ED}} \right\}, \quad (23)$$

where the $\mathbf{x}^{(i)} \in \mathbb{R}^{Q \times M}$ represents a collection of input excitations discretized on the time axis \mathcal{T} , and $\mathbf{y}^{(i)} = \mathcal{M}(\mathbf{x}^{(i)}) \in \mathbb{R}^Q$ is the corresponding discretized time response.

The set of coefficients \mathbf{c} in Eq. (22) is determined in a regression setting. By combining the set of *autoregressive lags* $y(t - (k + 1)\delta t)$ and *exogenous input lags* $x_i(t - k\delta t)$, we can assemble

the vector of regressive lags $\varphi(t)$ as:

$$\begin{aligned}\varphi(t) = & \{y(t - \delta t), y(t - 2\delta t), \dots, y(t - n_y \delta t), \\ & x_1(t), x_1(t - \delta t), \dots, x_1(t - n_{x_1} \delta t), \\ & \dots, \\ & x_M(t), x_M(t - \delta t), \dots, x_M(t - n_{x_M} \delta t)\},\end{aligned}\tag{24}$$

where the maximum number of time steps considered for each component $\{n_y, n_{x_1}, \dots, n_{x_M}\}$ are known as *model orders* (Billings, 2013).

For a given input/output pair $\{\mathbf{x}^{(i)}(t), y^{(i)}(t)\}$, e.g., a single element of the experimental design \mathbf{X} from Eq. (23), we introduce a so-called *design matrix* $\Phi \in \mathbb{R}^{\tilde{Q} \times n}$, with $n = n_y + \sum_{i=1}^M n_{x_i}$, which collects all the vectors of regressive lags $\varphi(t_i)$, as well as the corresponding model responses $y(t_i)$:

$$\Phi = \begin{pmatrix} \varphi(t_0) \\ \varphi(t_0 + \delta t) \\ \vdots \\ \varphi(t_0 + (Q-1)\delta t) \end{pmatrix}, \quad \mathbf{y} = \begin{pmatrix} y(t_0) \\ y(t_0 + \delta t) \\ \vdots \\ y(t_0 + (Q-1)\delta t) \end{pmatrix},\tag{25}$$

with $t_0 = \max(n_y, n_{x_1}, \dots, n_{x_M})\delta t$, and thus $\tilde{Q} = Q - t_0/\delta t$.

Finally, the design matrices from different input/output pairs from the experimental design in Eq. (23) can be assembled together into the design matrix Φ_{ED} :

$$\Phi_{\text{ED}} = \begin{pmatrix} \Phi^{(1)} \\ \vdots \\ \Phi^{(n_{\text{ED}})} \end{pmatrix}, \quad \mathbf{y}_{\text{ED}} = \begin{pmatrix} \mathbf{y}^{(1)} \\ \vdots \\ \mathbf{y}^{(n_{\text{ED}})} \end{pmatrix}.\tag{26}$$

It is now possible to estimate the set of model coefficients in Eq. (22) by solving the classical regression problem:

$$\hat{\mathbf{c}} = \arg \min_{\mathbf{c}} \mathcal{L}(\mathbf{y}_{\text{ED}}, \widehat{\mathcal{M}}(\Phi_{\text{ED}}; \mathbf{c})),\tag{27}$$

where $\mathcal{L}(\bullet, \bullet)$ is a suitable loss function, typically a quadratic error term. Arguably the most common form of autoregressive models is that of *linear-in-the-parameters* models (Billings, 2013), which causes Eq. (27) to take the well-known form of least squares regression:

$$\hat{\mathbf{c}} = \arg \min_{\mathbf{c}} \|\mathbf{y}_{\text{ED}} - \mathcal{G}(\Phi_{\text{ED}}) \mathbf{c}\|^2,\tag{28}$$

where $\mathcal{G} : \mathbb{R}^{|\Phi|} \rightarrow \mathbb{R}^{|\mathbf{c}|}$ is a generally nonlinear deterministic mapping between lags and regressors, such as multivariate polynomials, or a cosine basis. In its basic form, the classical ordinary least square in Eq. (28) admits an explicit solution:

$$\hat{\mathbf{c}} = (\Psi_{\text{ED}}^\top \Psi_{\text{ED}})^{-1} \Psi_{\text{ED}}^\top \mathbf{y}_{\text{ED}},\tag{29}$$

where $\Psi_{\text{ED}} \stackrel{\text{def}}{=} \mathcal{G}(\Phi_{\text{ED}})$.

Numerous advanced approaches exist for the solution of the optimization problem in Eq. (28), in particular sparsity-inducing regularized regression, also known as compressive sensing, *e.g.* least absolute shrinkage and selection operator (LASSO, [Tibshirani \(1996\)](#)), or least angle regression (LARS, [Efron et al. \(2004\)](#)).

Once the vector of parameters $\hat{\mathbf{c}}$ is estimated by regression from the available experimental design, the dynamic response of a model to a new, unseen exogenous input $\mathbf{x}^*(t)$ can be predicted iteratively from the one-step-ahead (OSA) predictor in Eq. (22), a process known as *model forecast*. More formally:

$$\hat{y}(t + \delta t) = \mathcal{G}(\varphi^*(t + \delta t)) \mathbf{c}, \quad (30)$$

where the vector of prediction regressive lags φ^* is constructed as follows:

$$\begin{aligned} \hat{\varphi}(t + \delta t) = & \{\hat{y}(t), \hat{y}(t - \delta t), \dots, \hat{y}(t - (n_y - 1)\delta t), \\ & x_1(t + \delta t), x_1(t), \dots, x_1(t - (n_{x_1} - 1)\delta t), \\ & \dots, \\ & x_M(t + \delta t), x_M(t), \dots, x_M(t - (n_{x_M} - 1)\delta t)\}, \end{aligned} \quad (31)$$

with each autoregressive lag $\hat{y}(t)$ built directly from Eq. (30). Because this prediction relies on the availability of a set of autoregressive lags even for the first timestep, it is common to initialize the first n_y timesteps of $\hat{y}(t)$ to $\{\hat{y}(0), \dots, \hat{y}((n_y - 1)\delta t)\} = 0$ or, for validation purposes, to the true model predictions ([Schär et al., 2024](#)).

4.3 Limitations of NARX modeling

While NARX has been proven to be accurate in multiple applied settings, it has two major limitations that can affect its usability in the context of uncertainty quantification:

- it can only represent a stationary system, *i.e.* its coefficients encode the behavior of a particular system under variable time-dependent excitations. A new model must be trained if the physical properties of the system are changed, even if the same excitations are considered. As an example, a classical NARX model cannot approximate the response of an oscillator with variable stiffness or geometry;
- the input/output map $\widehat{\mathcal{M}}(\bullet, \bullet)$ in Eq. (20) has in general finite complexity/expressivity, which in turn is connected to the size of the parameter vector \mathbf{c} . This makes strongly nonlinear maps difficult to approximate with relatively small experimental designs;
- complex computational models may depend on a large number of lags, causing the number of regressors in Eq. (28) to become unmanageably large. This is a common problem in surrogate modeling, known as the *curse of dimensionality*.

In the following sections, we introduce two state-of-the-art methods to solve the first two challenges in real world applications: polynomial-chaos NARX ([PC-NARX, Spiridonakos and](#)

Chatzi (2015b,a); Mai et al. (2016)) to handle model nonstationarity in Section 4.4, and manifold-NARX (mNARX, Schär et al. (2024)) to handle both highly nonlinear and high-dimensional maps in Section 4.5, respectively. The third challenge, related to the curse of dimensionality, is discussed in depth and tackled through a novel functional reformalization of NARX modeling, namely functional-NARX (F-NARX), in Schär et al. (2025), which lies outside the scope of this chapter.

4.4 Polynomial-chaos NARX

If the dynamical response of the system under consideration also depends on a set of M_ξ uncertain *structural parameters* $\xi \in \mathbb{R}^{M_\xi}$ with joint probability distribution $\xi \sim f_\Xi$, we can rewrite Eq. (20) as follows (Spiridonakos and Chatzi, 2015a):

$$y(t) = \mathcal{M}(\mathbf{x}(\mathcal{T} \leq t), \xi, \beta). \quad (32)$$

Because the components of ξ are not time-dependent, they cannot be used directly in the one-step-ahead formalism introduced in Eq. (22). As a consequence, Spiridonakos and Chatzi (2015a,b); Mai et al. (2016) propose to include the parametric variability directly in the coefficients of the one-step-ahead prediction in Eq. (22), by modifying it as follows:

$$\hat{y}(t + \delta t, \xi) = \widehat{\mathcal{M}}(\mathbf{x}(\mathcal{T} \leq t + \delta t), y(\mathcal{T} < t + \delta t), \mathbf{c}(\xi)) + \varepsilon(t), \quad (33)$$

where the explicit dependence on the initial conditions β has been dropped for notational simplicity. Intuitively, Eq. (33) represents a family of NARX models parametrized by the structural parameters ξ .

With this formalism, Spiridonakos and Chatzi (2015a,b) and Mai et al. (2016) propose a two-step approach to surrogate dynamic systems with variable structural parameters:

- create a surrogate model of the vector of model parameters $\hat{\mathbf{c}}(\xi) \approx \mathbf{c}(\xi)$ based on sparse polynomial chaos expansion (Blatman and Sudret, 2011; Mai et al., 2016):

$$\hat{c}_\kappa = \sum_{j=1}^{N_{c_\kappa}} a_j^\kappa \psi_j^\kappa(\xi), \quad (34)$$

where the ψ_j 's are multivariate polynomials suitably constructed from the joint probability distribution of the structural parameters (See Eq. (5));

- use the surrogated parameters in the standard NARX one-step-ahead predictor in Eq. (30), which now reads:

$$\hat{y}(t + \delta t) = \mathcal{G}(\varphi^*(t + \delta t)) \hat{\mathbf{c}}(\xi^*). \quad (35)$$

The training of a PC-NARX model from a given experimental design is quite similar to that of a classical NARX model (see Section 4.2), with the exception of an additional step to fit the

coefficients of the PCE model $\widehat{\mathbf{c}}(\boldsymbol{\xi})$. As a first step, the experimental design in Eq. (23) must now include the uncertain structural parameters $\boldsymbol{\xi}$:

$$\mathcal{X} = \left\{ \left(\mathbf{x}^{(i)}, \boldsymbol{\xi}^{(i)}, \mathbf{y}^{(i)} \right), i = 1, \dots, n_{\text{ED}} \right\}. \quad (36)$$

The second step is to train a separate autoregressive model for each element of the experimental design, without considering the structural parameters $\boldsymbol{\xi}$, by directly solving the least square problem as:

$$\mathbf{c}^{(i)} = \left(\boldsymbol{\Psi}^{(i)\top} \boldsymbol{\Psi}^{(i)} \right)^{-1} \boldsymbol{\Psi}^{(i)\top} \mathbf{y}^{(i)}, \quad (37)$$

with $\boldsymbol{\Psi}^{(i)} \stackrel{\text{def}}{=} \mathcal{G}(\boldsymbol{\Phi}^{(i)})$. For details on how to select a common regressor basis $\mathcal{G}(\bullet)$ for all the traces in the experimental design, an important step to ensure stability of the algorithm, the reader is referred to [Mai et al. \(2016\)](#).

Once the regression coefficients for each element of the experimental design is available, all what is needed to calculate the model predictions in Eq. (35) are the expansion coefficients $\mathbf{a}^\kappa = \{a_1^\kappa, \dots, a_{N_{c_\kappa}}^\kappa\}$ in Eq. (34). They are calculated separately for each autoregressive coefficient $\widehat{c}_\kappa(\boldsymbol{\xi})$ ([Spiridonakos and Chatzi, 2015a](#); [Mai et al., 2016](#)). We start by assembling the following experimental design:

$$\boldsymbol{\Xi}_{\text{ED}} = \begin{pmatrix} \boldsymbol{\xi}^{(1)} \\ \vdots \\ \boldsymbol{\xi}^{(n_{\text{ED}})} \end{pmatrix}, \quad \mathbf{c}_{\text{ED}}^\kappa = \begin{pmatrix} c_\kappa^{(1)} \\ \vdots \\ c_\kappa^{(n_{\text{ED}})} \end{pmatrix}. \quad (38)$$

Once the experimental design is available, state-of-the-art polynomial chaos expansion can be employed directly to calculate both the orthogonal polynomials (from the joint distribution of the structural parameters $f_{\boldsymbol{\Xi}}$) and the coefficients ([Blatman and Sudret, 2011](#); [Mai et al., 2016](#); [Lüthen et al., 2022](#)) needed to perform predictions on unseen data, following Eq. (35).

4.5 Manifold-NARX

Sometimes complex computational models can be strongly nonlinear, even in the absence of structural parameters, or may require a large number of exogenous inputs. A typical example of both these class of models is given by aero-servo-elastic simulators, which calculate the dynamic structural or functional response of a wind turbine, including its control system, to high-dimensional turbulent wind timeseries.

In this class of problems, the direct use of autoregressive models is essentially impossible, because the topological complexity of the mapping $\widehat{\mathcal{M}}(\bullet, \bullet)$ in Eq. (22) becomes intractable even with the most advanced learners available in the regression and machine-learning literature.

To address both of these problems, [Schär et al. \(2024\)](#) recently proposed *manifold-NARX* (mNARX), a variant of NARX that introduces a low-dimensional *autoregressive manifold*, on which $\widehat{\mathcal{M}}(\bullet, \bullet)$ becomes tractable. In more quantitative terms, the idea is that we want to substitute the original exogenous input \mathbf{x} in Eq. (20) with a manifold $\boldsymbol{\zeta}$, such that the new mapping

$\tilde{\mathcal{M}} : \zeta(\mathcal{T} \leq t) \rightarrow y(t)$ is less nonlinear, resulting in simpler and more accurate autoregressive models. This manifold is constructed iteratively by defining a sequence of auxiliary quantities $z_i(t)$, either by directly processing the exogenous input (e.g. through dimensionality reduction techniques), or by introducing additional physically meaningful intermediate quantities based on prior knowledge of the system (Schär et al., 2024):

$$\begin{aligned} z_1(t) &= \mathcal{F}_1(\mathbf{x}(\mathcal{T} \leq t), z_1(\mathcal{T} < t)) \\ z_2(t) &= \mathcal{F}_2(z_1(\mathcal{T} \leq t), \mathbf{x}(\mathcal{T} \leq t), z_2(\mathcal{T} < t)) \\ &\vdots \\ z_i(t) &= \mathcal{F}_i(z_1(\mathcal{T} \leq t), \dots, z_{i-1}(\mathcal{T} \leq t), \mathbf{x}(\mathcal{T} \leq t), z_i(\mathcal{T} < t)), \end{aligned} \tag{39}$$

where the $\mathcal{F}_i(\bullet, \bullet)$ represent arbitrarily complex functions. For example, to accurately predict the power output and other diagnostic quantities of interest of an operating wind turbine, Schär et al. (2024) used as $z_i(t)$ several spatial Fourier modes of exogenous input (high-dimensional, spatially coherent turbulent wind excitation), as well as additional autoregressive quantities extracted from the simulation data, such as the turbine's blade pitch (actuated by a controller), the blade azimuth, and the angular velocity of the rotor.

All of the $z_i(t)$ are then aggregated into the final exogenous input manifold $\zeta(t) = \{z_1(t), \dots, z_{M_\zeta}(t)\}$, which is substituted to \mathbf{x} in Eq. (22):

$$\hat{y}(t + \delta t) = \widehat{\mathcal{M}}(\zeta(\mathcal{T} \leq t + \delta t), y(\mathcal{T} < t + \delta t), \mathbf{c}) + \varepsilon(t). \tag{40}$$

From here, the surrogate training procedure is identical to that of classical NARX highlighted in Section 4.2. Predicting the response of an mNARX model on an unseen exogenous input is also very similar to the case of classical NARX in Eq. (30), with the additional step of projecting the unseen input onto the autoregressive manifold $\mathbf{x}^*(t) \rightarrow \zeta^*(t)$, through Eq. (39). For an in-depth discussion on the construction, strengths and limitations of mNARX, the reader is referred to Schär et al. (2024).

5 Application to a simple case study: coupled oscillator

We consider a coupled system with two masses, m_s and m_u , connected by a nonlinear spring with stiffness k_s and a linear damper c . The second mass m_s is also connected to the ground by a linear spring with stiffness k_u .

This system is governed by the following ordinary differential equations:

$$\begin{cases} m_u \ddot{y}_1(t) = k_s(y_2(t) - y_1(t))^3 + c(\dot{y}_2(t) - \dot{y}_1(t)) + k_u(x(t) - y_1(t)), \\ m_s \ddot{y}_2(t) = -k_s(y_2(t) - y_1(t))^3 - c(\dot{y}_2(t) - \dot{y}_1(t)). \end{cases} \tag{41}$$

The upper mass m_s is significantly smaller than the lower mass m_u , and the ratios $\frac{k_s}{m_s}$ and $\frac{k_u}{m_u}$ are of similar magnitude. Therefore, the displacement of m_s (y_2) is highly dependent on

that of m_u (y_1). Conversely, the displacement of m_u is largely unaffected by m_s . The system is subjected to a random excitation on m_u via the lower spring, defined as:

$$x(t) = \frac{1}{N_\omega} \sum_{i=1}^{N_\omega} A_i \sin(2\pi B_i t + C_i). \quad (42)$$

This excitation is the average of N_ω sinusoidal terms, where N_ω is a discrete uniform random variable from 1 to 10. Each term has a random amplitude $A_i \sim \mathcal{U}(-1, 1)$, frequency $B_i \sim \mathcal{U}(-1, 1)$, and phase $C_i \sim \mathcal{U}(-\pi, \pi)$, resulting in a highly varied family of signals, including both simple and complex excitations. Of interest is the displacement of the top mass m_s .

To showcase the different approximation capabilities of polynomial chaos-NARX and Manifold-NARX, we consider two different system configurations:

- strong damping with uncertain masses and springs, and
- weak damping with fixed masses and springs.

Each of these cases challenges classical NARX modeling differently: uncertainty in springs and masses results in variable system responses to the same excitation, breaking classical NARX assumptions on the fixed properties of the system. Conversely, weak damping causes the top mass response to be much more nonlinear, causing classical NARX to require a large number of lags, which can quickly result in an untreatable number of terms in Eq. (24).

High damping and variable system – PC-NARX

The first system is characterized by a relatively high damping coefficient, associated with significant variability in the system parameters. For reference, the parameter distributions are provided in Table 3.

Table 3: Distributions of the parameters of the highly damped oscillator in Section 5. All the parameters are normally distributed, with tabulated means μ_i and corresponding coefficients of variation σ_i/μ_i .

Parameter	Mean	Unit	$\text{CoV}_i = \sigma_i/\mu_i$
k_u	5,000	[N/m]	0.2
k_s	1,000	[N/m ³]	0.2
m_u	50	[kg]	0.2
m_s	10	[kg]	0.2
c	600	[N·m/s]	0.2

Classical NARX modeling is known to perform well in both system identification and surrogate modeling for a single realization of the system parameters. Nevertheless, the introduction

of variability in the system parameters is expected to cause classical NARX modeling to be insufficient to capture the complex nonlinear response of the system in Eq. (41).

In this case, a properly trained PC-NARX (Section 4.4) is expected to dynamically predict suitable NARX regression coefficients for each realization of the random system parameters, following Eqs. (34) and (35).

To assess the performance of both NARX and PC-NARX models, we train both models on the same set of $n_{ED} = 100$ independent realizations of both system parameters and excitation. For both methods, we use a polynomial NARX model up to degree $d = 3$, with $n_x = 5$ exogenous input and $n_y = 4$ autoregressive lags, respectively (see Eq. (31)). For classical NARX, the set of coefficients is calculated via ordinary-least-squares (OLS) over the entire training dataset. For PC-NARX, one set of coefficients is calculated for each of the trajectories in the experimental design. The resulting coefficients are then surrogated as a function of the input parameters $\mathbf{X} = \{k_u, k_s, m_u, m_s, c\}$ through an adaptive sparse PCE (Eq. (34)), with adaptive truncation up to $d_{PCE} = 10$ (Lüthen et al., 2022).

The comparative performance between the two surrogate modeling approaches is showcased in the two columns of Figure 3. The performance of a classical NARX model trained on the entire dataset is shown on the left column for two different out-of-sample simulations (rows). While it generally achieves discrete approximation performance, the NARX model tends to be inaccurate at the start of the trace, where the frequency content is generally richer, before the damper has time to dissipate enough energy. At later times, the discrepancy between the surrogate and the reference trace decreases significantly.

The performance of a PC-NARX trained on the same dataset is shown on the right column of Figure 3. The surrogate is highly accurate on both traces, even if a decrease in error over time comparable to classical NARX can still be observed. Despite the NARX component of PC-NARX being identical to that of its classical counterpart, the additional fine-tuning of the coefficients brought by the PCE component of the algorithm allows for a significant improvement in accuracy when the system parameters are uncertain.

Low damping and fixed system - mNARX

In this second scenario, we consider the same damped oscillator as in the previous section, but with two significant differences: i) there is no uncertainty on the system parameters, and ii) the damping coefficient c is strongly reduced. Their values are reported for reference in Table 4.

While removing the variability in the system parameters can in principle simplify the autoregressive problem, reducing the damping of over an order of magnitude causes the response of the upper mass to become much more complex to predict. However, its effect on the lower mass is relatively low, making the system an ideal candidate for the mNARX algorithm described in Section 4.5.

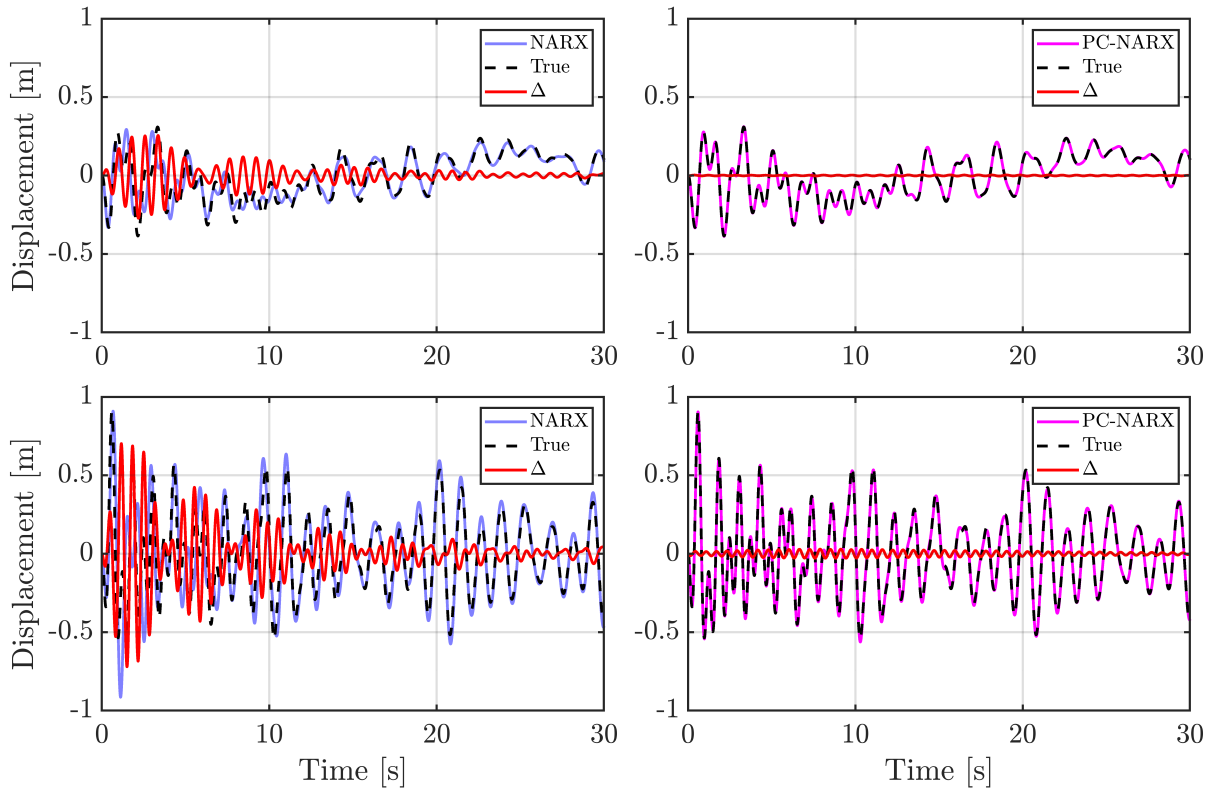


Figure 3: Comparison of classical NARX and PC-NARX surrogates on the strong-damping, uncertain parameters case study in Section 5. Each row represents an out-of-sample realization of both system parameters and exogenous input excitation. The left column shows the performance of classical polynomial NARX, while the right column shows that of PC-NARX. In all plots, the black dashed line is the reference validation signal, the blue line represents the NARX approximation, the magenta line represents the PC-NARX approximation, and the red line shows the corresponding approximation error $\Delta = \hat{y}(t) - y(t)$.

Table 4: Parameters of the weakly damped oscillator in Section 5.

Parameter	Value	Unit
k_u	5,000	[N/m]
k_s	1,000	[N/m ³]
m_u	50	[kg]
m_s	10	[kg]
c	50	[N·m/s]

To compare the accuracy of classical NARX and mNARX, we proceed as in Section 5, by building an experimental design of $n_{ED} = 100$ realizations of the exogenous input excitation, and fitting both models on the same dataset. An out-of-sample set of traces is used to test the accuracy of the two methods.

Due to the increased complexity in the displacement of m_u , we obtained the best results with a highly nonlinear NARX with maximum polynomial degree $d = 7$, and using $n_x = 3$ and $n_y = 4$ lags, respectively.

The left column of Figure 4 shows the performance of classical NARX on two out-of-sample realizations of the input excitation. While the overall features of the time series, such as the dominant frequency and the overall amplitude trends, are correctly approximated, the overall surrogate accuracy is still rather low. In contrast to the corresponding plots on the left column of Figure 3, no clear trend can be identified in the evolution of the approximation error over time, as the damping coefficient is too low to effectively dissipate high-frequency energy within this time scale.

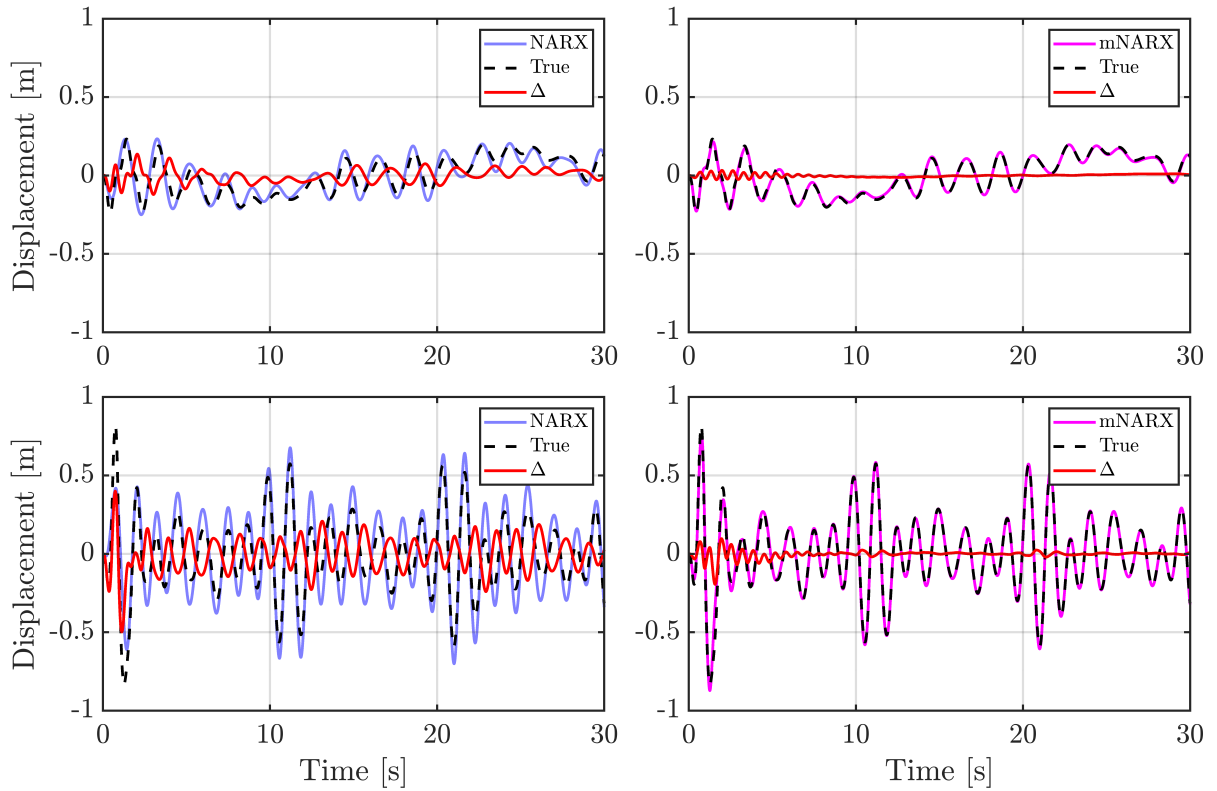


Figure 4: Comparison of classical NARX and mNARX surrogates on the weak-damping case study in Section 5. Each row represents an out-of-sample realization of both system parameters and exogenous input excitation. The left column shows the performance of classical polynomial NARX, while the right column shows that of mNARX. In all plots, the black dashed line is the reference validation signal, the blue line represents the NARX approximation, the magenta line represents the mNARX approximation, and the red line shows the corresponding approximation error $\Delta = \hat{y}(t) - y(t)$.

To construct the mNARX model, we take advantage of the of Eq. (41), and use the lower mass response $y_u(t)$ as an auxiliary quantity in Eq. (39). This allows us to distribute the autoregressive

model for $y_s(t)$ in a sequence of two simpler models:

$$\begin{aligned}\hat{y}_u(t) &= \hat{y}_u(t, x(\mathcal{T} \leq t)) \\ \hat{y}_s(t) &= \hat{y}_s(t, x(\mathcal{T} \leq t), \hat{y}_u(\mathcal{T} \leq t)).\end{aligned}\tag{43}$$

In other words, we enrich the input manifold of the upper mass m_s by including the autoregressive model of the lower mass m_u . This allows us to create two different autoregressive models, each with significantly lower complexity than the single NARX, as reported in Table 5. The

Table 5: Parameters of the mNARX model for each of the oscillator responses in Eq. (43).

Response	d	n_x	n_y
y_u	4	2	3
y_s	6	2	3

performance of the resulting surrogate is reported in the right column of Figure 4, on the same traces as for the classical NARX counterpart (left column). Using the much simpler response of the lower mass m_u highly simplifies the predictions on the response of the second mass, resulting in an overall dramatic decrease in approximation error, despite the much simpler model.

6 Conclusions

Uncertainty quantification has become increasingly widespread in the design and analysis of complex dynamical systems. Due to its stochastic nature, it often requires the repeated evaluation of expensive computational models, which has in turn created the need for efficient and accurate surrogate modeling strategies.

In this chapter, we provide a review of the state of the art in surrogate modeling for the uncertainty quantification of dynamical systems. The specific surrogate modeling choice is connected to the nature of the loading excitation, which can be either fundamentally simple or fundamentally complex (Section 3.1). Problems with fundamentally simple excitations can often be handled either directly with classical *time-frozen* surrogates (Section 3.1), which approximate each time step independently from the others by introducing principal component analysis for efficiency, or with more advanced techniques such as time or frequency warping (Section 3.3). Problems with fundamentally complex inputs require instead different surrogate modeling strategies, based on extensions of non-linear autoregressive modeling (Section 4), such as polynomial-chaos NARX (Section 4.4) or the recently developed manifold-NARX (Section 4.5).

References

Acuña, G., C. Ramirez, and M. Curilem (2012). Comparing NARX and NARMAX models using ANN and SVM for cash demand forecasting for ATM. In *The 2012 International Joint Conference on Neural Networks (IJCNN)*, pp. 1–6.

Aguirre, L. and S. Billings (1993). Relationship between the structure and performance of identified nonlinear polynomial models. Research report, The University of Sheffield.

Aversano, G., A. Bellemans, Z. Li, A. Coussement, O. Gicquel, and A. Parente (2019). Application of reduced-order models based on PCA & Kriging for the development of digital twins of reacting flow applications. *Computers & Chemical Engineering* 121, 422–441.

Billings, S. A. (2013). *Nonlinear system identification: NARMAX methods in the time, frequency, and spatio-temporal domains*. Chichester, West Sussex, United Kingdom: John Wiley & Sons, Inc.

Blatman, G. and B. Sudret (2011). Adaptive sparse polynomial chaos expansion based on least angle regression. *J. Comput. Phys.* 230(6), 2345–2367.

Blatman, G. and B. Sudret (2013). Sparse polynomial chaos expansions of vector-valued response quantities. In G. Deodatis (Ed.), *Proc. 11th Int. Conf. Struct. Safety and Reliability (ICOSSAR'2013)*, New York, USA, pp. 1–8.

Chen, S., X. X. Wang, and C. J. Harris (2008). NARX-based nonlinear system identification using orthogonal least-squares basis hunting. *IEEE Transactions on Control Systems Technology* 16(1), 78–84.

Chevreuil, M., R. Lebrun, A. Nouy, and P. Rai (2015). A least-squares method for sparse low rank approximation of multivariate functions. *SIAM/ASA Journal Uncertainty Quantification* 3(1), 897–921.

Choi, M., T. P. Sapsis, and G. E. Karniadakis (2014). On the equivalence of dynamically orthogonal and bi-orthogonal methods: Theory and numerical simulations. *Journal of Computational Physics* 270, 1–20.

Coca, D. and S. A. Billings (2001). Non-linear system identification using wavelet multiresolution models. *International Journal of Control* 74(18), 1718–1736.

Deshmukh, A. P. and J. T. Allison (2017). Design of dynamic systems using surrogate models of derivative functions. *Journal of Mechanical Design* 139(10), 101402.

Doostan, A., A. Validi, and G. Iaccarino (2013). Non-intrusive low-rank separated approximation of high-dimensional stochastic models. *Computer Methods in Applied Mechanics and Engineering* 263, 42–55.

Efron, B., T. Hastie, I. Johnstone, and R. Tibshirani (2004). Least angle regression. *The Annals of Statistics* 32(2), 407 – 499.

Gao, Y., S. Liu, F. Li, and Z. Liu (2016). Fault detection and diagnosis method for cooling dehumidifier based on LS-SVM NARX model. *International Journal of Refrigeration* 61, 69–81.

Garg, S., H. Gupta, and S. Chakraborty (2022). Assessment of DeepONet for reliability analysis of stochastic nonlinear dynamical systems. arXiv:2201.13145.

Gerritsma, M., J.-B. van der Steen, P. Vos, and G. Karniadakis (2010). Time-dependent generalized polynomial chaos. *Journal of Computational Physics* 229(22), 8333–8363.

Ghanem, R. and P. Spanos (2003). *Stochastic Finite Elements: A Spectral Approach* (2nd ed.). Courier Dover Publications, Mineola.

Ghanem, R. G. and P. D. Spanos (1991). *Stochastic finite elements – A spectral approach*. Springer Verlag, New York. (Reedited by Dover Publications, Mineola, 2003).

Goodfellow, I., Y. Bengio, and A. Courville (2016). *Deep learning*. MIT Press Ltd.

Guo, Y., S. Mahadevan, S. Matsumoto, S. Taba, and D. Watanabe (2023). Investigation of surrogate modeling options with high-dimensional input and output. *AIAA Journal* 61(3), 1334–1348.

Hu, Z., J. Fang, R. Zheng, M. Li, B. Gao, and L. Zhang (2024). Efficient model predictive control of boiler coal combustion based on NARX neural network. *Journal of Process Control* 134, 103158.

Jolliffe, I. T. (2002). *Principal component analysis* (2 ed.). Springer Series in Statistics. New York: Springer Verlag (Second Edition).

Jonkman, J. (2009). TurbSim User's Guide: Version 1.50. Technical report, National Renewable Energy Laboratory.

Kocijan, J. (2012). Plenary lecture 1: Dynamic GP models: An overview and recent developments. In *Proceedings of the 6th International Conference on Applied Mathematics, Simulation, Modelling*, ASM'12, Stevens Point, Wisconsin, USA, pp. 12. World Scientific and Engineering Academy and Society (WSEAS).

Konakli, K. and B. Sudret (2016a). Global sensitivity analysis using low-rank tensor approximations. *Reliability Engineering & System Safety* 156, 64–83.

Konakli, K. and B. Sudret (2016b). Polynomial meta-models with canonical low-rank approximations: Numerical insights and comparison to sparse polynomial chaos expansions. *Journal of Computational Physics* 321, 1144–1169.

Langeron, Y., K. T. Huynh, and A. Grall (2021). A root location-based framework for degradation modeling of dynamic systems with predictive maintenance perspective. *Proceedings of the Institution of Mechanical Engineers, Part O: Journal of Risk and Reliability* 235(2), 253–267.

Le Maître, O. P., L. Mathelin, O. M. Knio, and M. Y. Hussaini (2010). Asynchronous time integration for polynomial chaos expansion of uncertain periodic dynamics. *Discrete and Continuous Dynamical Systems* 28(1), 199–226.

Levin, A. and K. Narendra (1996). Control of nonlinear dynamical systems using neural networks. II. Observability, identification, and control. *IEEE Transactions on Neural Networks* 7(1), 30–42.

Li, D., J. Zhou, and Y. Liu (2021). Recurrent-neural-network-based unscented Kalman filter for estimating and compensating the random drift of mems gyroscopes in real time. *Mechanical Systems and Signal Processing* 147, 107057.

Luchtenburg, D. M., S. L. Brunton, and C. W. Rowley (2014). Long-time uncertainty propagation using generalized polynomial chaos and flow map composition. *Journal of Computational Physics* 274, 783–802.

Lüthen, N., S. Marelli, and B. Sudret (2021). Sparse polynomial chaos expansions: Literature survey and benchmark. *SIAM/ASA Journal on Uncertainty Quantification* 9(2), 593–649.

Lüthen, N., S. Marelli, and B. Sudret (2022). Automatic selection of basis-adaptive sparse polynomial chaos expansions for engineering applications. *Int. J. Uncertainty Quantification* 12(3), 49–74.

Mai, C. and B. Sudret (2017). Surrogate models for oscillatory systems using sparse polynomial chaos expansions and stochastic time warping. *SIAM/ASA Journal on Uncertainty Quantification* 5(1), 540–571.

Mai, C.-V. (2016). *Polynomial chaos expansions for uncertain dynamical systems. Applications in earthquake engineering*. Ph. D. thesis, ETH Zürich, Switzerland.

Mai, C.-V., M. D. Spiridonakos, E. Chatzi, and B. Sudret (2016). Surrogate modeling for stochastic dynamical systems by combining nonlinear autoregressive with exogeneous input models and polynomial chaos expansions. *International Journal of Uncertainty Quantification* 6(4), 313–339.

Mattson, S. G. and S. M. Pandit (2006). Statistical moments of autoregressive model residuals for damage localisation. *Mechanical Systems and Signal Processing* 20(3), 627–645.

Meles, G. A., S. Marelli, and N. Linde (2025). Bayesian full waveform inversion with sequential surrogate model refinement. *Geophysical Journal International*. Submitted.

Murphy, K. P. (2012). *Machine Learning: A Probabilistic Perspective*. Adaptive Computation and Machine Learning Series. Cambridge, Massachusetts, USA: The MIT Press.

Murray-Smith, R., T. A. Johansen, and R. Shorten (1999). On transient dynamics, off-equilibrium behaviour and identification in blended multiple model structures. In *1999 European Control Conference*, pp. 3569–3574. IEEE.

Nagel, J., J. Rieckermann, and B. Sudret (2020). Principal component analysis and sparse

polynomial chaos expansions for global sensitivity analysis and model calibration: application to urban drainage simulation. *Reliability Engineering & System Safety* 195(106737).

Ranković, V., N. Grujović, D. Divac, and N. Milivojević (2014). Development of support vector regression identification model for prediction of dam structural behaviour. *Structural Safety* 48, 33–39.

Rasmussen, C. E. and C. K. I. Williams (2006). *Gaussian processes for machine learning* (Internet ed.). Adaptive computation and machine learning. Cambridge, Massachusetts: MIT Press.

Rezaeian, S. and A. Der Kiureghian (2010). Simulation of synthetic ground motions for specified earthquake and site characteristics. *Earthquake Engineering & Structural Dynamics* 39(10), 1155–1180.

Samsuri, N. A., S. A. Raman, and T. M. Y. S. Tuan Ya (2023). Evaluation of NARX network performance on the maintenance application of rotating machines. In F. Ahmad, H. H. Al-Kayiem, and W. P. King Soon (Eds.), *ICPER 2020*, pp. 593–609. Springer Nature Singapore.

Santner, T. J., B. J. Williams, and W. I. Notz (2003). *The Design and Analysis of Computer Experiments*. Springer, New York.

Sapsis, T. and P. Lermusiaux (2009). Dynamically orthogonal field equations for continuous stochastic dynamical systems. *Physica D: Nonlinear Phenomena* 238(23), 2347–2360.

Schär, S. (2025). *Autoregressive surrogate modeling for dynamical systems*. Ph. D. thesis, ETH Zurich (Switzerland).

Schär, S., S. Marelli, and B. Sudret (2024). Emulating the dynamics of complex systems using autoregressive models on manifolds (mNARX). *Mechanical Systems and Signal Processing* 208, 110956.

Schär, S., S. Marelli, and B. Sudret (2025). Surrogate modeling with functional nonlinear autoregressive models (F-NARX). *Reliability Engineering & System Safety*, 111276.

Siegelmann, H., B. Horne, and C. Giles (1997). Computational capabilities of recurrent NARX neural networks. *IEEE Transactions on Systems, Man, and Cybernetics, Part B (Cybernetics)* 27(2), 208–215.

Smola, A. J. and B. Schölkopf (2004). A tutorial on support vector regression. *Statistics and Computing* 14, 199–222.

Song, H., X. Shan, L. Zhang, G. Wang, and J. Fan (2022). Research on identification and active vibration control of cantilever structure based on NARX neural network. *Mechanical Systems and Signal Processing* 171, 108872.

Spiridonakos, M. and E. Chatzi (2015a). Metamodelling of dynamic nonlinear structural systems through polynomial chaos NARX models. *Computers & Structures* 157, 99–113.

Spiridonakos, M. D. and E. N. Chatzi (2015b). Metamodeling of nonlinear structural systems with parametric uncertainty subject to stochastic dynamic excitation. *Earthquakes and Structures* 8(4), 915–934.

Tibshirani, R. (1996). Regression shrinkage and selection via the lasso. *Journal of the Royal Statistical Society. Series B (Methodological)* 58(1), 267–288.

Wagner, P.-R., R. Fahrni, M. Klippel, A. Frangi, and B. Sudret (2020). Bayesian calibration and sensitivity analysis of heat transfer models for fire insulation panels. *Engineering Structures* 205(110063).

Wan, X. and G. E. Karniadakis (2005). An adaptive multi-element generalized polynomial chaos method for stochastic differential equations. *Journal of Computational Physics* 209(2), 617–642.

Worden, K., W. Becker, T. Rogers, and E. Cross (2018). On the confidence bounds of Gaussian process NARX models and their higher-order frequency response functions. *Mechanical Systems and Signal Processing* 104, 188–223.

Xiu, D. (2010). *Numerical Methods for Stochastic Computations: A Spectral Method Approach*. Princeton, New Jersey, USA: Princeton University Press.

Xiu, D. and G. E. Karniadakis (2002, January). The Wiener-Askey polynomial chaos for stochastic differential equations. *SIAM Journal on Scientific Computing* 24(2), 619–644.

Yaghoubi, V., S. Marelli, B. Sudret, and T. Abrahamsson (2017). Sparse polynomial chaos expansions of frequency response functions using stochastic frequency transformation. *Probabilistic Engineering Mechanics* 48, 39–58.

Yu, C., Y.-P. Zhu, H. Luo, Z. Luo, and L. Lei (2023). Design assessments of complex systems based on design oriented modelling and uncertainty analysis. *Mechanical Systems and Signal Processing* 188(109988).

Zhang, J., Z. Yin, and R. Wang (2017). Nonlinear dynamic classification of momentary mental workload using physiological features and NARX-model-based least-squares support vector machines. *IEEE Transactions on Human-Machine Systems* 47(4), 536–549.

Zhang, Y., Y. Dong, and M. Beer (2024). rLSTM-AE for dimension reduction and its application to active learning-based dynamic reliability analysis. *Mechanical Systems and Signal Processing* 215, 111426.

Zhou, J. and J. Li (2023). An efficient time-variant reliability analysis strategy embedding the NARX neural network of response characteristics prediction into probability density evolution method. *Mechanical Systems and Signal Processing* 200, 110516.